SAR Image Change Detection via Heterogeneous Graph With Multiorder and Multilevel Connections

Jun Wang, *Member, IEEE*, Fei Zeng, Sanku Niu, Jun Zheng, and Xiaoliang Jiang

***Abstract*—Synthetic aperture radar (SAR) image change detection is currently a popular topic, but the existence of speckle noise renders it challenging. Making full use of the neighborhood information can reduce noise interference and improve accuracy. To this end, this study proposes a graph-guided method for SAR image change detection. First, we establish the local, nonlocal, and global connections according to three types of neighboring rules. A novel heterogeneous graph is then constructed by assigning different weights to these multilevel connections. On the basis of heterogeneous graph, a composite random walk matrix (CRWM) is presented to quantify the similarity of multilevel connections. Thereafter, the heterogeneous graph shift system consisting of the multiorder CRWM is designed to aggregate the attributes of neighboring vertices along the multiorder and multilevel connections. The change measure can be implemented by comparing the output signals from the heterogeneous graph shift systems, resulting in the generation of difference image with good separability. Finally, change analysis is carried out using a binary classification algorithm. Experiments conducted on six real SAR datasets confirm that the proposed M2HG method successfully strikes a balance between speckle suppression and change enhancement. This strategic balance translates into improvements in performance metrics, with OA, κ, and $F1$ indicators surpassing those of the suboptimal method by 0.87%, 3.34%, and 3.84%, respectively. Overall, the proposed method emerges as a promising contender for SAR image change detection tasks.**

***Index Terms*—Change detection, composite random walk matrix (CRWM), heterogeneous graph, heterogeneous graph shift system, synthetic aperture radar (SAR).**

I. Introduction

CHANGE detection between synthetic aperture radar (SAR) images is a significant technique for finding changes in the same scene but at different times [1]. Since imaging with SAR sensors is independent of atmospheric conditions, SAR image change detection has received considerable attention in the field of agricultural surveys [2], urban studies [3], environmental monitoring [4], hazard assessment [5], and other Earth observations [6], [7], [8]. However, the distinctive imaging principle of SAR sensors causes serious speckle noise in SAR images, leading to image distortion that poses challenges for change detection [9].

In unsupervised SAR image change detection, three crucial steps are executed in sequence [10]:

1) preprocessing;
2) change measure;
3) change analysis.

The preprocessing step aims at aligning the bitemporal SAR images into the same spatial–spectral domain using radiometric correction and registration. The change measure step intends to identify the attribute differences between SAR images and produce the difference image. During change analysis, a binary classifier is employed to segment the difference image into unchanged and changed areas so as to obtain final change maps. Indeed, achieving precise SAR image change detection outcomes is typically fraught with difficulties due to the lack of spectral features compounded by the pervasive interference of speckle noise. Therefore, this study concentrates on change enhancement and noise suppression during the change measure process, aiming to generate difference images with good separability.

Early studies on change measures focus primarily on pixel-based methods, with the subtraction and ratio operators being the two classical ones. Among them, the ratio operator is considered more appropriate for processing coherent SAR image information. The log-ratio (LR) operator is the most commonly used pixel-based change measure method since the logarithmic operation can convert the multiplicative speckle noise to an additive one [11]. These pixel-based methods may be suitable for the noise-free images, but the inherent characteristic of SAR images, specifically the multiplicative speckle noise, suggests otherwise. To reduce the interference from speckle noise, scholars propose the neighborhood-based methods for SAR image change measure. The mean-ratio (MR) operator, which uses the local means of neighboring pixels as study units, typically performs better than classic pixel-based methods [12]. However, MR sometimes fails instead when comparing the neighbors with similar local means but dissimilar intensity distributions. To tackle this problem, the neighborhood-based ratio (NR) operator utilizes the spatial information and the local variance to optimize change measure [13]. Moreover, several studies present a discrete wavelet transform (DWT) based fusion strategy that integrates the changes detected by MR and

Manuscript received 20 December 2023; revised 4 March 2024 and 14 April 2024; accepted 21 May 2024. Date of publication 24 May 2024; date of current version 19 June 2024. This work was supported in part by the National Natural Science Foundation of China under Grant 62101206, in part by the Key Research and Development Program of Zhejiang Province under Grant 2021C02021, and in part by the Zhejiang Provincial Natural Science Foundation of China under Grant LZY22D010001. *(Corresponding authors: Xiaoliang Jiang; Jun Wang.)*

Jun Wang, Fei Zeng, Sanku Niu, and Xiaoliang Jiang are with the School of Mechanical Engineering, Quzhou University, Quzhou 324000, China (e-mail: 36110@qzc.edu.cn; 221122020478@zjut.edu.cn; niusanku@qzc.edu.cn; jxl_swjtu@163.com).

Jun Zheng is with the School of Information Engineering, Huangshan University, Huangshan 245000, China (e-mail: 105370@hsu.edu.cn).

Digital Object Identifier 10.1109/JSTARS.2024.3405170

© 2024 The Authors. This work is licensed under a Creative Commons Attribution-NonCommercial-NoDerivatives 4.0 License. For more information, see https://creativecommons.org/licenses/by-nc-nd/4.0/

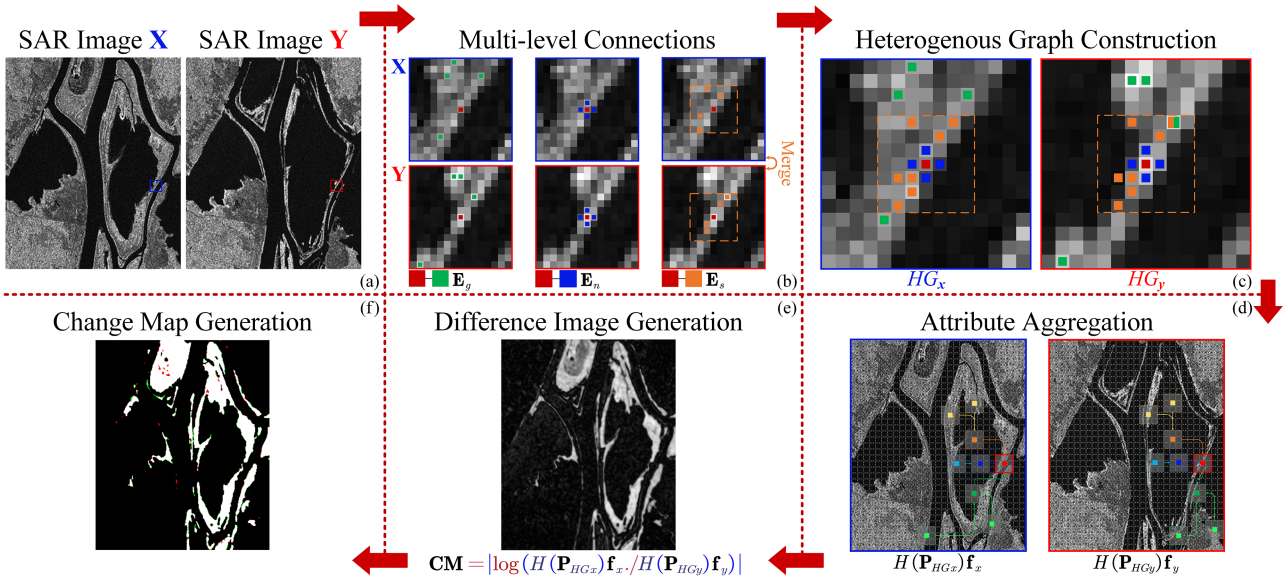

Fig. 1. Workflows of the proposed M2HG method.

LR operators to improve the separability of difference image [14], [15]. Since the patch can describe the local characteristics of an image, researchers use the probability density functions (PDFs) to determine the statistical differences between patches, leading to the development of SAR image change detection method. In [16] and [17], a range of PDF estimation methods is explored to generate difference image by applying the Kullback–Leibler divergence for PDF comparisons. Inspired by the nonlocal theory [18], the nonlocal mean-ratio (NLMR) method is proposed, which makes use of the similarities of neighboring patches to create smooth difference images [19]. Furthermore, a method using ratio-based nonlocal information (RNLI) is proposed for SAR image change detection. The RNLI is quantified by the similarity of two patches within the nonlocal neighborhood, and the similarity can be well characterized by the ratio-based Gaussian kernel function [20]. Derived from image filtering principles, these methods employ the characteristics of surrounding pixels to smooth the studied pixel, effectively diminishing the speckle noise interference in change detection. Nevertheless, the dense neighborhood introduces the information redundancy and oversmoothing issues. In addition, there has been insufficient attention devoted to excavate the discriminative features regarding changes.

To circumvent this drawback, scholars favor graph-based change measure methods as they enable more efficient utilization of neighborhood information through flexible graph structures [21], [22], [23], [24]. In [25], a weighted graph containing sparse neighborhood information is designed to identify the changes of local extreme keypoints. Moreover, a pointwise change detection method is implemented through the stereograph, which connects the local maximum pixels on bitemporal SAR images and captures the multispan neighborhood information from the edges to enhance the change measure [26]. Scholars also develop a dual-layer graph to combine the nonlocal neighborhood information of both intensity and texture attributes for noise suppression and change measure [27]. In addition, an improved nonlocal patch-based graph (INLPG) is proposed for change detection in which each image patch is taken as a vertex and is connected to its nonlocal neighbors. Change measure is achieved by comparing the weights on the edges [28]. These graph-based methods, which leverage the inherent properties of graph structures to integrate neighborhood information, have proved efficacy in suppressing speckle noise within SAR images. However, the reliance on low-order neighborhoods constrains the receptive field of these methods. Moreover, the failure to exploit neighborhood information for change enhancement leads to a lessened capability for identifying changes in complex scenarios. Therefore, it is imperative to develop a more effective pattern that optimally constructs and utilizes neighborhood to improve SAR image change detection.

In this study, a novel SAR image change detection method based on the heterogeneous graph with multilevel and multiorder connections (M2HG) is proposed. The main contributions are as follows.

1) First of all, a heterogeneous graph is rigorously designed based on multilevel connections rather than single connection, in order to effectively capture the complex neighborhood information among similar pixels in the whole image. With respect to the graph structure, three types of edges representing multilevel connections are constructed by traversing the local, nonlocal, and global neighbors. This allows for a wider receptive field for the heterogeneous graph, and thus, the description and discrimination of ground objects could be enhanced.
2) From the constructed heterogeneous graph, a composite random walk matrix (CRWM) is proposed to quantify the similarity of multilevel connections. A heterogeneous graph shift system, represented by the combination of the multiorder CRWM, is then designed to aggregate the attributes of neighboring vertices along the multiorder and

multilevel connections. The difference image with good separability can be created by comparing the bitemporal output signals through the systems.

3) Indeed, the M2HG can be considered as a generalization neighborhood-based change detection framework. Many related methods, such as MR, NLMR, and INLPG, can be realized by simplifying or adjusting the graph structures of M2HG. Comparative experiments involving these related change detection methods are conducted on six real SAR datasets to demonstrate the effectiveness of the proposed M2HG. For convenience, the source code of the M2HG is available.[1]

The rest of this article is organized as follows. In Section II, the detailed elaboration of our proposed M2HG change detection method is provided. A series of comparative experiments are conducted in Section III. Finally, Section IV concludes this article.

II. Proposed Algorithm

Denote two SAR images, collected before and after a surface activity in the same geographical scene, by $\mathbf{X}$ and $\mathbf{Y}$, respectively. This study is to use heterogeneous graphs to establish multilevel connections between similar vertices and quantify these connections into the graph characteristic matrix. Then, a heterogeneous graph shift system, represented by the polynomials of the graph characteristic matrix, is applied to aggregate the attributes of neighboring vertices along the multilevel connections. Change measure is performed by comparing the aggregated attributes so as to generate the difference image. Finally, binary classification is adopted to generate the final change map. Fig. 1 gives the outline of the proposed M2HG change detection method.

A. Graph Characteristic and Graph Shift System

Graph theory has been proven to be effective in describing neighborhood information through the use of graph characteristic matrices [29], [30], [31], [32], [33]. Let $G = \{V, E, \omega\}$ be an ordinary graph in which N vertices are connected by the edges E and the associated weights ω refer to the similarity between vertices. All the weights can be summarized as an N-by-N weighted adjacency matrix $\mathbf{W}$, defined by

$$W_{ij} = \begin{cases} \omega(V_i, V_j); & \text{if}(V_i, V_j) \in E \\ 0; & \text{if}(V_i, V_j) \notin E. \end{cases} \tag{1}$$

Since the graph is undirected, the matrix $\mathbf{W}$ is symmetric and the element $\omega(V_i, V_j)$ equals $\omega(V_j, V_i)$. Normalizing the weighted adjacency matrix $\mathbf{W}$ to gain the random walk matrix $\mathbf{P} = \mathbf{D}^{-1}\mathbf{W}$, where $\mathbf{D}$ is a diagonal matrix representing the degree of vertices, and its ith element is $D_{ii} = \Sigma_j W_{ij}$.

Suppose $\mathbf{f} = \{f(i) \in \mathbb{R}, i = 1, \ldots, N\}$ is the feature signal on the graph, which together with the matrices above can be formed as some important graph characteristics

$$(\mathbf{Wf})(i) = \sum_{j \sim i} \omega(V_i, V_j) f(j) \tag{2}$$

$$(\mathbf{Pf})(i) = \frac{1}{\sum_{j \sim i} \omega(V_i, V_j)} \sum_{j \sim i} \omega(V_i, V_j) f(j). \tag{3}$$

In a weighted graph, each connected vertex diffuses its own information to adjacent vertices, and at the same time, it also receives diffusion information from other vertices according to the weighting function. This characteristic makes the graph an efficient tool for not only describing signal information but also comprehending the intrinsic structure of signals. From this perspective, the graph characteristics $(\mathbf{Wf})(i)$ and $(\mathbf{Pf})(i)$ can be considered as the aggregation of the information from adjacent vertices to the studied vertex i. In detail, the graph characteristic $\mathbf{Wf}$ can be considered as a weighted information aggregator executed in the vertex domain, and $\mathbf{Pf}$ is the normalized version of this aggregator. Here, the graph shift operator $\mathbf{S}$ is utilized to uniformly represent the graph characteristic matrices $\mathbf{W}$ and $\mathbf{P}$. Then, a graph shift system, consisting of the polynomials of graph shift operators $\mathbf{S}$, is defined as

$$H(\mathbf{S}) = h_0\mathbf{S}^0 + h_1\mathbf{S}^1 + \cdots + h_M\mathbf{S}^M = \sum_{m=0}^{M} h_m\mathbf{S}^m \tag{4}$$

where $h_0, h_1, \ldots, h_M$ are the coefficients, and $\mathbf{S}^m$ represents the m-order graph shift operator. The introduction of multiorder aggregators implies the stacking of receptive field, enabling a wider aggregation of information. Referring to (2) and (3), the aggregated output signal through the graph shift system is

$$\mathbf{f}_{\text{out}} = H(\mathbf{S})\mathbf{f} = \sum_{m=0}^{M} h_m\mathbf{S}^m\mathbf{f}. \tag{5}$$

With the support of an effective graph structure, the beneficial information can be captured and aggregated through the graph shift system to assist in achieving change detection tasks.

B. Heterogeneous Graph Construction

Heterogeneous graph is a generalization of the ordinary graph that allows for the definition of various types of vertices or edges [34], [35], [36]. This makes the heterogeneous graph ideal for representing a wide variety of relationships between vertices. Therefore, we take the original pixels as vertices and connect them based on three neighboring rules in order to construct the heterogeneous graph with an effective structure. Denote $HG = \{V, E_g, E_s, E_n, \omega_g, \omega_s, \omega_n\}$, then we have

$$V \Leftrightarrow \mathbf{I}; |V| = N \tag{6}$$

$$E_g = \{(p, q); q \in \text{GSN}(p)\} \tag{7}$$

$$E_s = \{(p, q); q \in \text{STCN}(p)\} \tag{8}$$

$$E_n = \{(p, q); q \in \text{K}^+\text{NN}(p)\} \tag{9}$$

where V is the vertex set, and N is the total number of pixels.

E_g is the global edge formed by connecting the vertex with its global similar neighbors (GSNs). The GSN is represented as follows:

$$\text{GSN}(p) = \{\varphi_c(p) \cup p\} \tag{10}$$

[1][Online]. Available: https://github.com/JunWangZJ/M2HG_CD.git

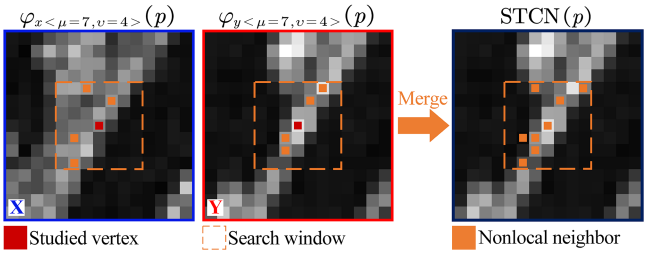

Fig. 2. Schematic for nonlocal edge construction. The search window is set to 7×7 and the number of similar neighbors is $v = 4$.

where $\varphi_c(p)$ is the similar neighbor for vertex p across the entire image. This set is composed of the c smallest elements extracted from the distance ensemble $\{\text{dist}[f(p), f(l)] \mid l = 1, \ldots, p-1, p+1, \ldots, N\}$. Here, the function dist$(\cdot,\cdot)$ is defined as the Euclidean distance metric. According to the self-expression property, each pixel or patch can be approximately reconstructed by other similar ones in the image [37]. Therefore, the changes of each pixel or patch can be measured with the help of their corresponding similar neighbors. In detail, if there is no change between the studied bitemporal pixels, the global edge-connected pixels should also remain unchanged. Conversely, if changes occur in the studied pixels, the global similar pixels would also undergo changes. Furthermore, the accumulated changes of these similar vertices can be aggregated along the global edges and utilized to enhance the changes of the studied vertex. This is the motivation for us to construct the global edges E_g.

E_s represents the nonlocal edge, which is connected based on the spatial–temporal coupled neighbors (STCNs). The STCN is defined as follows:

$$\text{STCN}(p) = \{\varphi_{x<\mu,v>}(p) \cup \varphi_{y<\mu,v>}(p) \cup p\} \tag{11}$$

where $\varphi_{x<\mu,\ v>}(p)$ denotes the set of v most similar vertices within a $\mu \times \mu$ search window centered at vertex p in SAR image $\mathbf{X}$, so is $\varphi_{y<\mu,\ v>}$ from the SAR image $\mathbf{Y}$. Both similarity measures are computed based on the Euclidean distance metric. The STCN(p) is then constructed by merging the vertex p with the corresponding sets $\varphi_{x<\mu,\ v>}(p)$ and $\varphi_{y<\mu,\ v>}(p)$. A schematic for nonlocal edge construction is given in Fig. 2. In fact, we construct the nonlocal edge E_s, which is inspired by nonlocal theory and intends to utilize the attributes of the vertices connected by it for speckle suppression. Moreover, the construction of nonlocal edges E_s can filter out the pixels in dense windows that are weakly correlated with the studied pixel. This also helps to prevent information redundancy and oversmoothing in the subsequent change measure.

E_n represents the local edge and is constructed based on the K^+ nearest neighbors (K^+NN). The K^+NN is defined as follows:

$$\text{K}^+\text{NN}(p) = \{\text{KNN}(p) \cup p\} \tag{12}$$

where KNN(p) is the K nearest neighbors of the vertex p. As changes never occur in isolation, the nearest neighbors are highly informative in determining whether the studied pixel has changed.

After the topology of the graph has been determined, the weights should be assigned to the corresponding edges. The weights are typically calculated using Euclidean distance or Gaussian distance of the intensity [25]. Nevertheless, these distances may not be effective enough for SAR images that contain noise. Inspired by the probabilistic patch-based (PPB) filter [38], a modified noniteration PPB weight is adopted here to measure the similarity between vertices of the heterogeneous edges. The weight is determined by comparing the two neighbor sets $\varphi_k(p)$ and $\varphi_k(q)$, which are around the vertices p and q, respectively. Therefore, the weight ω_s of the nonlocal edge is expressed as follows:

$$\omega_s(p,q) = \exp\left\{-\sum \log\left(\frac{\varphi_k(p)}{2\varphi_k(q)} + \frac{\varphi_k(q)}{2\varphi_k(p)}\right)\right\} \tag{13}$$

where $\varphi_k(p)$ is the k nearest neighbors around the vertex p, so is $\varphi_k(q)$. The value of parameter k is fixed at 8 empirically. In fact, there exist some similarities between global and nonlocal edges as they both connect pixels within a larger receptive field. Hence, the weight ω_g of the global edge can be also calculated by (13).

For the local edge, the weight ω_n is defined as follows:

$$\omega_n(p,q) = \frac{1}{|\text{STCN}(p)|} \sum_{(p,q)\in E_s} \omega_s(p,q) \tag{14}$$

where $|\text{STCN}(p)|$ represents the total number of vertices within STCN(p). Here, the weight ω_n is set as the average of ω_s to ensure numerical balance. After the weights are assigned, the heterogeneous graph has been constructed. We design three types of edges based on different theoretical perspectives to establish multilevel connections between pixels, providing an effective structure for heterogeneous graph. Fig. 1(b) and (c) records the construction of the multilevel connections and heterogeneous graph.

According to the above definition of heterogeneous graph, we construct the heterogeneous graphs on the bitemporal SAR images, respectively. Then, a change measure can be performed by comparing the comprehensive attributes from each vertex and its multilevel neighbors. It should be noted that the two heterogeneous graphs possess the same topology for local and nonlocal edges, but their global edges differ from each other. The local and nonlocal neighbors with the same topology are used to suppress the speckle noise and achieve a smooth measurement. The global neighbors with different topologies are used to amplify the changes. This is the main difference between our method and many other graph-based change detection methods that rely on the same graph structure but different input signals.

C. Change Measure Based on Heterogeneous Graph With Multiorder and Multilevel Connections

In general, the structure of a graph can be quantified as a weighted adjacency matrix or random walk matrix [25], [27]. The elements of these characteristic matrices reflect the correlation between paired pixels. Therefore, we develop a characteristic matrix for heterogeneous graph to describe the proposed multilevel connections and utilize it for change detection tasks. Here, a CRWM $\mathbf{P}_{\text{HG}}$ for the proposed heterogeneous graph is

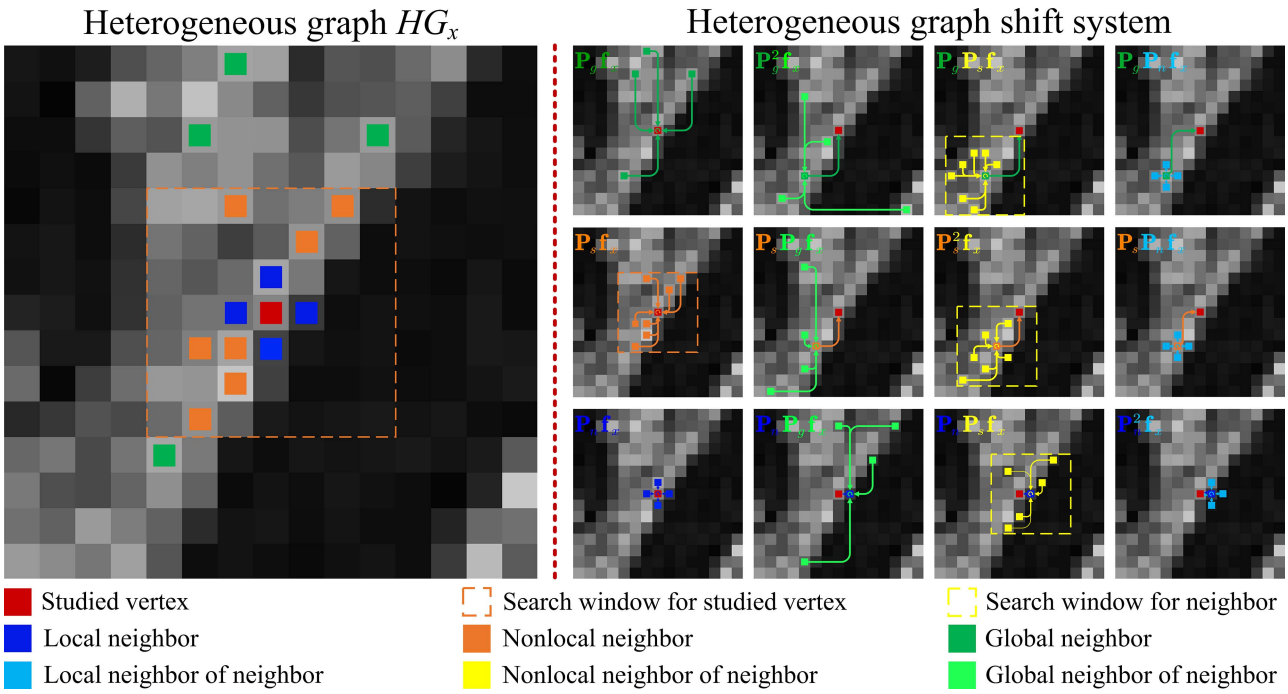

Fig. 3. Schematic of the heterogeneous graph (left) and shift system (right). The search window is set to 7 × 7 and the number of neighbors is set to $K = c = v = 4$.

designed as follows:

$$\mathbf{P}_{\mathrm{HG}} = \mathbf{P}_n + \mathbf{P}_s + \mathbf{P}_g \tag{15}$$

where $\mathbf{P}_n$ represents the local random walk matrix for the local edge E_n. $\mathbf{P}_s$ is the nonlocal random walk matrix for the nonlocal edge E_s, and $\mathbf{P}_g$ is the global random walk matrix for the global edge E_g. The matrix $\mathbf{P}_{\mathrm{HG}}$ comprises these three matrices and can be used to quantify the multilevel connections in the heterogeneous graph.

Let the shift operator $\mathbf{S} = \mathbf{P}_{\mathrm{HG}}$, the novel heterogeneous graph shift system can be constructed as follows:

$$\begin{aligned} H(\mathbf{P}_{\mathrm{HG}}) &= h_0\mathbf{P}_{\mathrm{HG}}^0 + h_1\mathbf{P}_{\mathrm{HG}}^1 + h_2\mathbf{P}_{\mathrm{HG}}^2 \\ &= h_0\mathbf{I} + h_1\mathbf{P}_{\mathrm{HG}} + h_2\mathbf{P}_{\mathrm{HG}}^2. \end{aligned} \tag{16}$$

In this study, the first three-order operators are adopted to construct the multiorder and multilevel connections for each vertex. As a result, the heterogeneous graph shift system is regarded as a composite aggregator that gathers the attributes of neighbor vertices along the multiorder and multilevel connections. The zero-order operator is an identity matrix that captures only the own attributes of each vertex. As there is speckle noise in these attributes, we set the coefficient $h_0 = 0$. This does not imply that the original attributes of each vertex are completely discarded. Instead, they are embedded into high-order operators through the proposed self-loop edges $\mathbf{E}_g$, $\mathbf{E}_s$, and $\mathbf{E}_n$. In order to achieve a balanced integration of information contributed by one-order and two-order neighbors, the remaining system coefficients are empirically set as $h_1 = h_2 = 1$. Then, the shift system can be simplified as follows:

$$\begin{aligned} H(\mathbf{P}_{\mathrm{HG}}) = \mathbf{P}_{\mathrm{HG}} + \mathbf{P}_{\mathrm{HG}}^2 &= \mathbf{P}_g + \mathbf{P}_s + \mathbf{P}_n + (\mathbf{P}_g + \mathbf{P}_s + \mathbf{P}_n)^2 \\ &= \mathbf{P}_g + \mathbf{P}_s + \mathbf{P}_n + \mathbf{P}_g^2 + \mathbf{P}_s^2 + \mathbf{P}_n^2 \\ &\quad + \mathbf{P}_g\mathbf{P}_s + \mathbf{P}_g\mathbf{P}_n + \mathbf{P}_s\mathbf{P}_g + \mathbf{P}_s\mathbf{P}_n + \mathbf{P}_n\mathbf{P}_g + \mathbf{P}_n\mathbf{P}_s. \end{aligned} \tag{17}$$

In detail, $\mathbf{P}_g$, $\mathbf{P}_s$, and $\mathbf{P}_n$ serve as the information aggregators based on one-hop neighbors. Likewise, $\mathbf{P}_g^2$, $\mathbf{P}_s^2$, and $\mathbf{P}_n^2$ can be regarded as the high-order aggregators that depend on two-hop neighbors, while the remaining rely on cross-hop neighbors. Therefore, the heterogeneous graph shift system enables the combination of the attributes from multilevel and multiorder neighboring vertices, thereby facilitating change detection. Fig. 3 illustrates a schematic of the heterogeneous graph and shift system. The number of neighbors is set to $K = c = v = 4$. Due to the specificity of STCN, the quantity of nonlocal neighbors may fluctuate between 4 and 8. The attributes of neighboring vertices are aggregated layer-by-layer toward the studied vertex, following the arrow directions in the schematic.

Construct two heterogeneous graphs HGx and HGy on bitemporal SAR images, respectively. Denote $\mathbf{f}_x = [f_1, \ldots, f_N]^{\mathrm{T}}$ as the attribute vector for all vertices in the SAR image $\mathbf{X}$, so is $\mathbf{f}_y$ for the SAR image $\mathbf{Y}$. $H(\mathbf{P}_{\mathrm{HG}x})$ and $H(\mathbf{P}_{\mathrm{HG}y})$ are the two heterogeneous graph shift systems with different weights in the SAR images. The change measure of M2HG can be implemented by comparing the output signals through the heterogeneous graph shift systems and is defined as follows:

$$\mathbf{CM} = \left|\log\left(H(\mathbf{P}_{\mathrm{HG}_x})\mathbf{f}_x./H(\mathbf{P}_{\mathrm{HG}_y})\mathbf{f}_y\right)\right|. \tag{18}$$

The difference image of M2HG can be generated by mapping the $\mathbf{CM}$ onto the original SAR image dimensions. Fig. 1(d) presents the schematic of information aggregation $H(\mathbf{P}_{\mathrm{HG}x})\mathbf{f}_x$

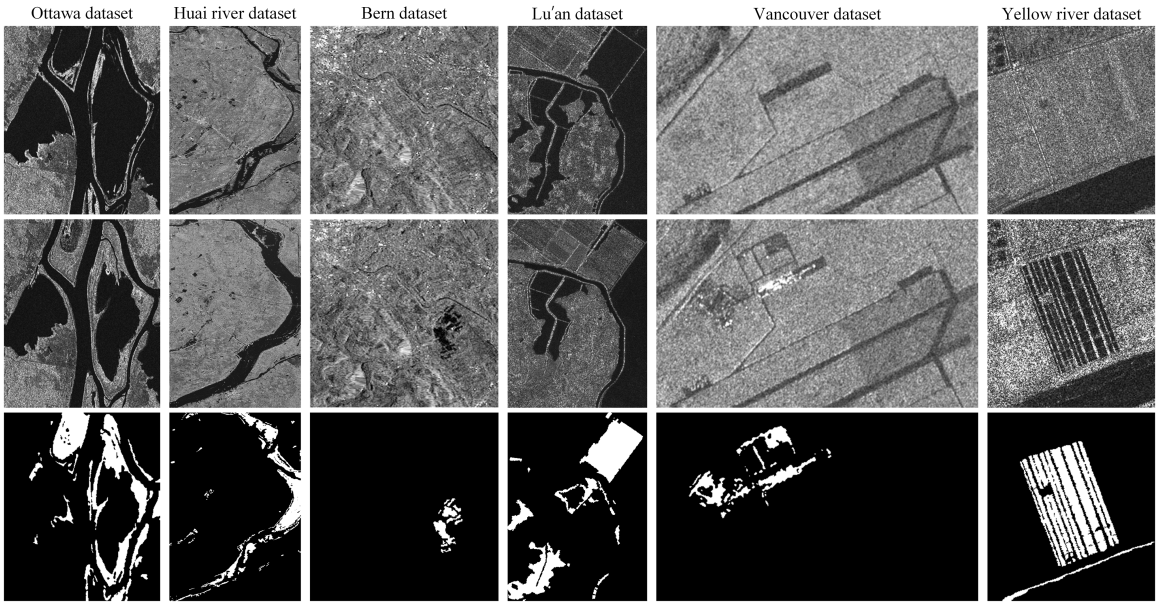

Fig. 4. Six experimental SAR datasets. From the first row to the third row refer to the SAR image **X**, the SAR image **Y**, and the ground truth, respectively.

and $H(\mathbf{P}_{\mathrm{HG}\,y})\mathbf{f}_y$, and Fig. 1(e) depicts the generation of difference image. Indeed, many neighborhood-based methods, such as MR, NLMR, and INLPG, can be realized using a shift system with different graph structures or input attributes. For example, the MR operator is equivalent to a one-order local shift operation based on the image grid. The NLMR operator can be viewed as a one-order nonlocal shift operation that is achieved by considering all vertices' attributes in the search window. Moreover, INLPG uses the Laplace matrix as the shift operator based on nonlocal neighbors. Therefore, the proposed M2HG can be considered a change detection framework based on the generalization neighborhood, which has great research value and development potential. Finally, the binary classification algorithm is applied to segment the difference image into unchanged and changed portions, thus generating the change map.

III. Experimental Study

In this section, the comparative experiments are conducted on six real SAR datasets to verify the effectiveness of the proposed M2HG method. First, in the form of grayscale images, the difference image generated by M2HG is qualitatively compared with those derived from the six change measure methods. Then, the Otsu threshold [39] is applied to obtain change maps, and the performance of generated difference images is validated through quantitative analysis. Finally, five effective change detection methods are utilized to comparatively evaluate the effectiveness of the M2HG method in combination with the superior classifier.

A. Experimental Setup

As shown in Fig. 4, six real SAR datasets acquired from different sensors are adopted for the evaluation experiments. These datasets encompass a variety of ground changes related to flooding, building, and land cover. The bitemporal images of each SAR dataset are coregistered under one pixel by data preprocessing experts using specialized software, and the relevant prior information is detailed in Table I. For difference image comparison, we implemented several representative methods, including LR, MR [12], NR [13], DWT [14], NLMR [19], and INLPG [28]. To further verify the effectiveness of the proposed M2HG, change detection analyses are conducted using graph cuts (GCs) method [41], principal component analysis with K-means (PCA-K) clustering method [42], fuzzy clustering with a modified Markov random field (MRFFCM) method [43], principal component analysis network (PCANet) method [44], and convolutional-wavelet neural networks (CWNNs) method [45]. Among these methods, GC, PCA-K, and MRFFCM represent traditional unsupervised change detection methods that rely on inherent image features without requiring explicit training labels. In contrast, PCANet and CWNN are contemporary methods using artificial neural networks for machine learning, which are trained and guided by pseudolabels derived from unsupervised clustering algorithms. We integrate M2HG with GC (M2HG-GC) and CWNN (M2HG-CWNN) separately for change analysis to explore the validity of M2HG under different classifier frameworks.

For parameter settings, larger values are recommended for GSN and STCN in order to capture a greater number of global and nonlocal neighbors. To prevent oversmoothing, it is suggested to limit the number of local neighbors to a reasonable range, typically between 10 and 50. We establish the correlations among the parameters of M2HG to simplify the parameter setting process. Specifically, the number of both global and nonlocal neighbors is set to $c = v = 2K$. The size of search window is set to the smallest odd number that is strictly greater than $\sqrt[2]{4v}$. Therefore, the number of local neighbors for K^{+}NN is the only parameter that needs to be manually set. In the experiments, we set the local neighbors to $K = 50$ for Yellow River dataset and $K = 25$ for other datasets. For the MR, NR,

TABLE I
PRIOR INFORMATION OF SIX SAR DATASETS

Dataset	Ottawa	Huai river	Bern	Lu'an	Vancouver	Yellow river
Sensor	Radarsat-1	GaoFen-3	ERS-2	Sentinel-1	Radarsat-2	Radarsat-2
Polarization	HH	HH	VV	HV	HH	HH
Resolution (m)	10	5	30	10	3	8
ENLs	12.50 and 12.60	3.12 and 2.62	10.89 and 9.26	2.56 and 3.14	4.57 and 4.75	4.00 and 1.00
	July1997	June 2017	April1999	July 2015	June 2008	June 2008
	August1997	September 2017	May1999	October 2015	November 2009	June 2009
Size	290 × 350	554 × 780	301 × 301	429 × 580	908 × 532	257 × 289
Change	Flood event	Flood event	Flood event	Land cover	Building	Land cover

DWT, NLMR, and INLPG methods, the patch sizes ranging from 3×3 to 11×11 are tested in the initial experiments. The suitable sizes are recorded in the experimental analysis of each dataset. Moreover, the search window of NLMR is fixed as 11×11 based on the initial results. The patch interval and adjacency rate for INLPG are calculated based on the guidelines from the literature [28], concurrently taking the predetermined patch size into account. Parameters for the five change detection methods are set following their respective research articles.

B. Evaluation Criteria

As there are ground-truth images for the SAR datasets, the experimental results can be evaluated quantitatively. We count the actual number of pixels for the unchanged class (N_u) and the changed class (N_c), respectively. The unchanged pixels are labeled as negative and the changed pixels are labeled as positive to construct the confusion matrix. Among that, the false positive (FP) represents the number of unchanged pixels that are misclassified as changed, while the false negative (FN) represents the number of changed pixels that are mistakenly classified as unchanged. The true positive (TP) and true negative (TN), respectively, refer to the number of changed and unchanged pixels that are correctly detected. Moreover, the overall accuracy (OA) and kappa coefficient (κ) are employed for comprehensive evaluations, and the definitions are presented as follows:

$$\mathrm{OA} = \frac{\mathrm{TP} + \mathrm{TN}}{\mathrm{TP} + \mathrm{FP} + \mathrm{TN} + \mathrm{FN}} \tag{19}$$

$$\kappa = \frac{\mathrm{OA} - \mathrm{PRE}}{1 - \mathrm{PRE}} \tag{20}$$

where

$$\mathrm{PRE} = \frac{(\mathrm{TP} + \mathrm{FN}) \times N_c + (\mathrm{TN} + \mathrm{FP}) \times N_u}{(\mathrm{TP} + \mathrm{FP} + \mathrm{TN} + \mathrm{FN})^2}. \tag{21}$$

$F1$ score is also adopted to evaluate the classification performance, which is defined as follows:

$$F1 = \frac{2 \times \mathrm{precision} \times \mathrm{recall}}{\mathrm{precision} + \mathrm{recall}} \tag{22}$$

where

$$\mathrm{precision} = \frac{\mathrm{TP}}{\mathrm{TP} + \mathrm{FP}}, \quad \mathrm{recall} = \frac{\mathrm{TP}}{\mathrm{TP} + \mathrm{FN}}. \tag{23}$$

C. Performance Analysis of Difference Image Generation

This experiment aims to assess the effectiveness of the proposed M2HG in generating difference images. The first dataset is collected by the RADARSAT-1 sensor on different dates in Ottawa city. It consists of two SAR images that reflect the backscatter changes during flooding rise and recession periods. The initial results show that the 3×3 patch size for MR, NR, DWT, NLMR, and INLPG is suitable for the Ottawa dataset. Difference images generated by seven methods (LR, MR, NR, DWT, NLMR, INLPG, and the proposed M2HG) are shown in Fig. 5. Correspondingly, the seven change maps segmented using the Otsu thresholding are also presented. As observed, the LR method produces a dim difference image with poor separability. Numerous clustered spots can be seen in the background areas of MR and NR difference images, which makes it difficult to distinguish the real unchanged areas. Therefore, the change maps produced by these three methods contain a large number of false detections in the unchanged areas. The NLMR yields a smooth difference image, indicating its effectiveness in speckle suppression. However, it exhibits limitations in accurately describing the boundaries of changed areas. The DWT also lacks accuracy in boundary description since its difference image is coarse. The difference image of INLPG is flat but dim, and the contrast between unchanged and changed areas requires improvement. The difference image of M2HG presents good separability, revealing apparent intensity differences between the changed and unchanged areas. Table II lists the quantitative results for the seven change maps, and the optimal scores are marked in bold. The M2HG method has the lowest FN, with only 217, and its OA, κ, and $F1$ criteria are 0.22%, 0.60%, and 0.74%, respectively, higher than the second-best method. The improved accuracy achieved by the M2HG method stems from its intricate multiorder and multilevel connections. This sophistication, although beneficial for performance, inevitably results in a heavier computation requirement. Therefore, among the tested methods on the Ottawa dataset, M2HG exhibits the longest computation time at 214.04 s.

The second dataset comprises SAR images acquired by the GaoFen-3 sensor over the Anhui section of the Huai River, illustrating surface changes of the Huai River during dry and rainy seasons. For this dataset, a patch size of 5×5 is uniformly adopted for MR, NR, DWT, NLMR, and INLPG, which employs a patch size of 7×7. The difference images and change maps generated by the seven methods are presented in Fig. 6. Intuitively, the unchanged areas of LR, MR, NR, and

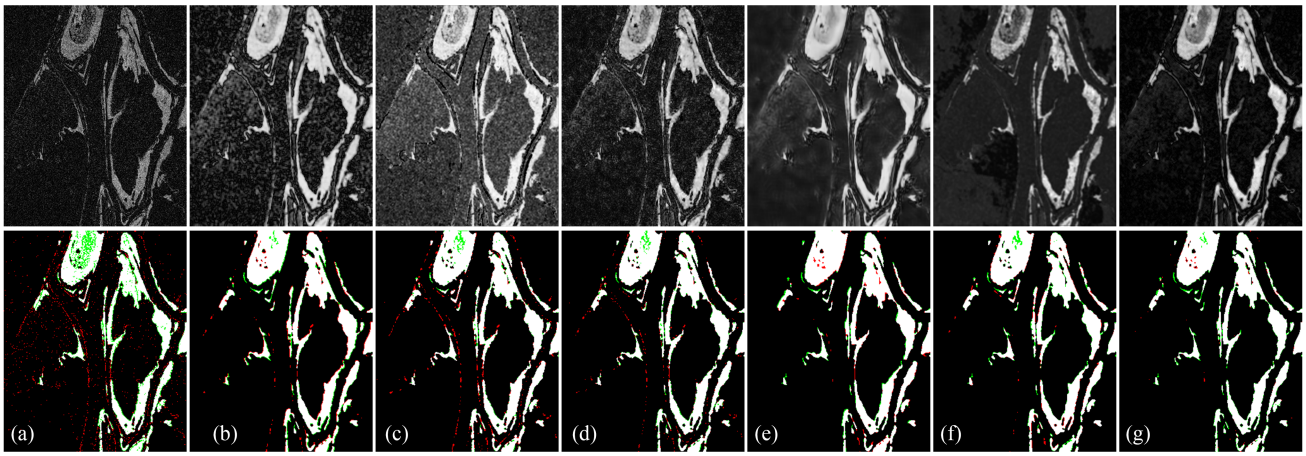

Fig. 5. Difference images (first row) and change maps (second row) of seven experimental methods on the Ottawa dataset. (a) LR. (b) MR. (c) NR. (d) DWT. (e) NLMR. (f) INLPG. (g) M2HG. In the change maps, White: TP; Black: TN; Green: FN; and Red: FP.

TABLE II
RESULTS OF CHANGE MEASURE METHODS ON OTTAWA AND HUAI RIVER DATASETS

Method	Ottawa						Huai river					
	FN	FP	OA	F1	κ	Time (s)	FN	FP	OA	F1	κ	Time (s)
LR	2741	2087	0.9524	0.8465	0.8183	**1.13**	5519	7642	0.9690	0.8078	0.7910	**1.32**
MR	1476	1292	0.9727	0.9133	0.8971	1.33	**2840**	11349	0.9666	0.8105	0.7924	1.58
NR	**763**	1281	0.9799	0.9373	0.9253	5.37	3787	8201	0.9717	0.8306	0.8153	17.36
DWT	1012	817	0.9820	0.9427	0.9320	6.23	3431	7408	0.9745	0.8459	0.8320	18.91
NLMR	914	724	0.9839	0.9487	0.9391	2.02	4044	6405	0.9754	0.8480	0.8346	6.38
INLPG	1092	687	0.9825	0.9439	0.9335	52.81	7452	**1567**	0.9787	0.8509	0.8395	33.78
M2HG	1192	**217**	**0.9861**	**0.9547**	**0.9465**	221.04	4672	2815	**0.9824**	**0.8839**	**0.8744**	1132.52

DWT are uneven, which poses a challenge for the classifier to distinguish between changed and unchanged areas. As a result, a large number of unchanged pixels are incorrectly classified as changed ones in their change maps. The result of NLMR is too smooth to accurately describe the boundaries of changed areas. The difference images of INLPG and M2HG show clear separability between changed and unchanged areas. However, the INLPG is deficient in reflecting the details of real changes, leading to the omission of many changed areas. In comparison, the change map of M2HG presents a closer approximation to the ground truth. Table II exhibits the quantitative results. The M2HG outperforms the second-best method in terms of OA, κ, and $F1$ criteria by 0.37%, 3.30%, and 3.49%, respectively. The M2HG method also incurs considerable computational time on the Huai River dataset due to its intricate connections. This burden is further exacerbated by the larger number of pixels in this dataset, resulting in a computation time of 1132.52 s. A consistent pattern of high time cost is observed across other datasets under evaluation.

The third dataset is collected by the ERS-2 satellite under a large width over the Bern city. The ground-truth image contains merely 1155 real changed pixels, accounting for just 1.27% of the total pixels in the image. Meanwhile, the minimum connected component within the image consists of only 13 pixels. Therefore, this dataset is particularly suitable for validating the ability in identifying small changed areas. To ensure that no small areas are missed, the patch sizes of MR, NR, DWT, NLMR, and INLPG are all uniformly set to 3×3 in this dataset. Seven difference images and their corresponding change maps are exhibited in Fig. 7. The results of LR, MR, and NR are still messy due to the disturbance of speckle noise, indicating that their capabilities of noise suppression need improvement. The NLMR and INLPG present smooth difference images, but the boundaries of the changed areas are blurred, which leads to detection errors. The difference images obtained from DWT and M2HG methods present good separability, revealing apparent differences between the changed and unchanged areas. However, the results of M2HG show a flatter background compared with DWT since M2HG incorporates multiorder and multilevel neighborhood information. As a result, M2HG achieves the highest OA, κ, and $F1$ of 0.9984, 0.8668, and 0.8652, respectively.

The fourth dataset is collected by the Sentinel-1 sensor and describes the land changes around Lu'an city. For this dataset, the patch sizes of MR, NR, DWT, and NLMR are set to 5×5, and INLPG utilizes a patch size of 7×7. The qualitative results of seven change measure methods are shown in Fig. 8, and the quantitative results are presented in Table III. The change maps of LR, MR, NR, and DWT all exhibit numerous isolated spots, which are attributed to the chaotic background areas within their

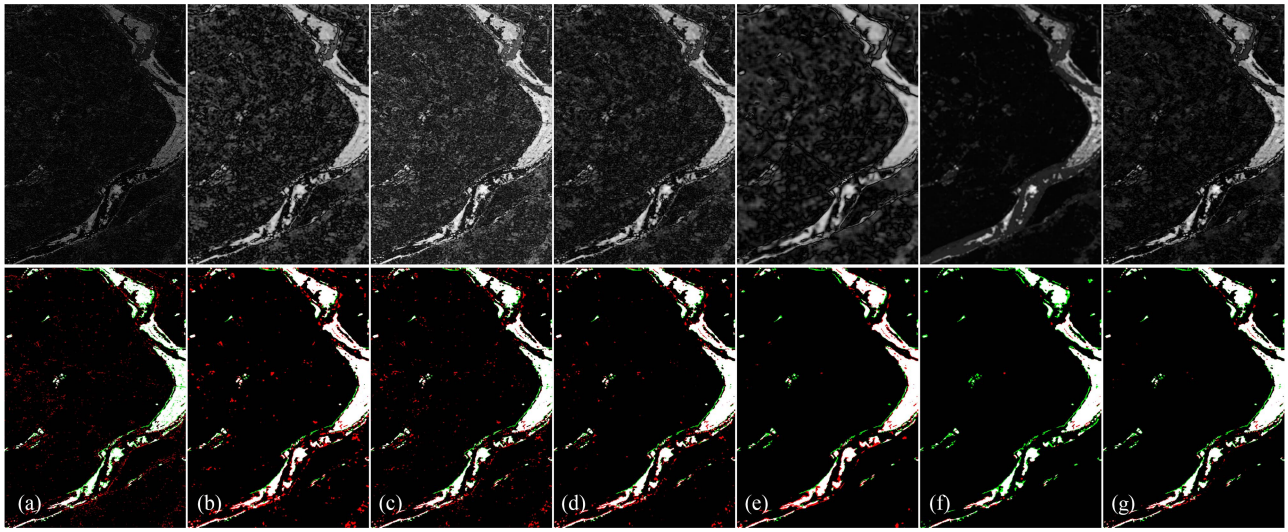

Fig. 6. Difference images (first row) and change maps (second row) of seven experimental methods on the Huai River dataset. (a) LR. (b) MR. (c) NR. (d) DWT. (e) NLMR. (f) INLPG. (g) M2HG. In the change maps, White: TP; Black: TN; Green: FN; and Red: FP.

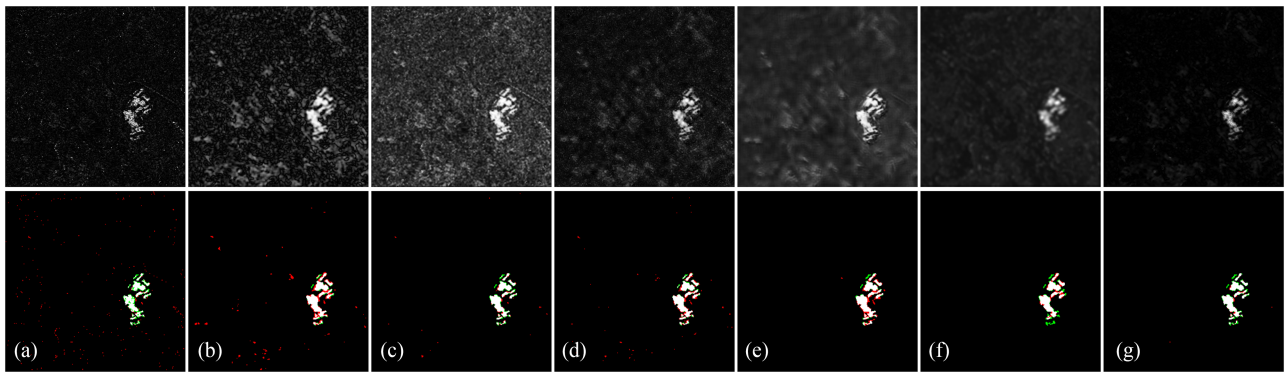

Fig. 7. Difference images (first row) and change maps (second row) of seven experimental methods on the Bern dataset. (a) LR. (b) MR. (c) NR. (d) DWT. (e) NLMR. (f) INLPG. (g) M2HG. In the change maps, White: TP; Black: TN; Green: FN; and Red: FP.

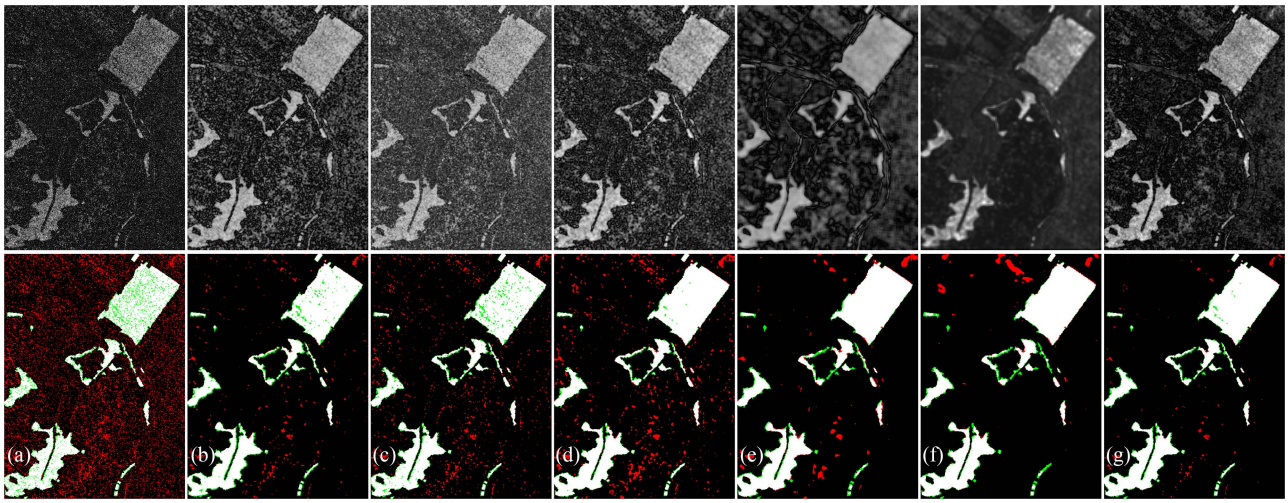

Fig. 8. Difference images (first row) and change maps (second row) of seven experimental methods on the Lu'an dataset. (a) LR. (b) MR. (c) NR. (d) DWT. (e) NLMR. (f) INLPG. (g) M2HG. In the change maps, White: TP; Black: TN; Green: FN; and Red: FP.

TABLE III
RESULTS OF CHANGE MEASURE METHODS ON BERN AND LU'AN DATASETS

Method	Bern						Lu'an					
	FN	FP	OA	F1	κ	Time (s)	FN	FP	OA	F1	κ	Time (s)
LR	321	368	0.9924	0.7077	0.7038	**0.94**	5668	28739	0.8617	0.6511	0.5707	**1.25**
MR	115	607	0.9920	0.7423	0.7384	1.12	3279	8048	0.9545	0.8590	0.8320	1.41
NR	195	134	0.9964	0.8537	0.8519	3.61	4728	6222	0.9560	0.8578	0.8318	10.12
DWT	**102**	333	0.9952	0.8288	0.8264	5.57	**2763**	8399	0.9551	0.8625	0.8359	11.43
NLMR	121	243	0.9960	0.8503	0.8483	1.82	3599	3622	0.9710	0.9044	0.8873	4.12
INLPG	232	187	0.9954	0.8150	0.8127	41.87	3893	2943	0.9725	0.9083	0.8922	12.91
M2HG	215	**74**	**0.9984**	**0.8668**	**0.8652**	182.52	3617	**1456**	**0.9796**	**0.9308**	**0.9189**	626.23

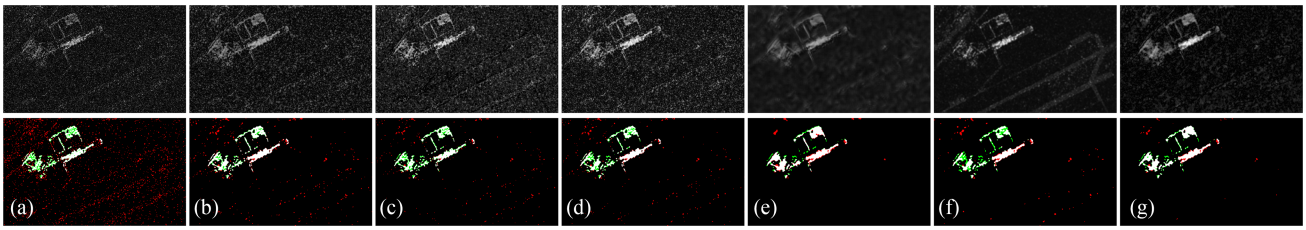

Fig. 9. Difference images (first row) and change maps (second row) of seven experimental methods on the Vancouver dataset. (a) LR. (b) MR. (c) NR. (d) DWT. (e) NLMR. (f) INLPG. (g) M2HG. In the change maps, White: TP; Black: TN; Green: FN; and Red: FP.

TABLE IV
RESULTS OF CHANGE MEASURE METHODS ON VANCOUVER AND YELLOW RIVER DATASETS

Method	Vancouver						Yellow River					
	FN	FP	OA	F1	κ	Time (s)	FN	FP	OA	F1	κ	Time (s)
LR	999	4597	0.9537	0.4764	0.4550	**1.25**	5426	11262	0.7753	0.4897	0.3514	**0.78**
MR	540	1356	0.9843	0.7602	0.7522	1.31	3069	5721	0.8817	0.7022	0.6291	0.92
NR	943	801	0.9856	0.7490	0.7416	7.32	4331	4358	0.8830	0.6769	0.6055	3.12
DWT	823	892	0.9858	0.7604	0.7531	8.75	3466	2996	0.9130	0.7552	0.7023	4.87
NLMR	**511**	652	0.9904	0.8392	0.8342	2.43	2783	2001	0.9356	0.8166	0.7776	1.35
INLPG	1154	724	0.9844	0.7180	0.7101	71.16	2057	1403	0.9534	0.8680	0.8397	14.74
M2HG	523	**414**	**0.9922**	**0.8658**	**0.8618**	263.25	**1237**	**1304**	**0.9658**	**0.9056**	**0.8848**	268.58

respective difference images. The NLMR demonstrates robust regional integrity, but it lacks clarity in boundary description. The INLPG displays flat difference images but fails to identify some linear changed areas, indicating a high miss-detection rate for this method. The proposed M2HG method generates a difference image that exhibits good separability, and the resulting change map accurately reflects real changes. Quantitatively, the M2HG method gains the lowest FP (1456) and the highest $F1$ (0.9308). It stands out as the sole method among the evaluated methods with a κ indicator exceeding 0.9.

The fifth dataset is acquired at Vancouver airport by the Radarsat-2 sensor. The narrow structure of the new building poses a challenge for change detection. To minimize the potential impact of registration inaccuracies, we downsample the images and adjust their dimensions to 454×266 pixels. A uniform patch size of 3×3 is applied to all comparison methods, and the results are presented in Fig. 9 and Table IV. The LR, MR, NR, and DWT methods yield difference images with blurred change features superimposed on a cluttered background. This visual ambiguity hinders the accurate identification of real changes, leading to numerous false detections. Although keeping a decent level of contrast, the difference image produced by INLPG exhibits the pseudochanges of the runway. Both NLMR and M2HG methods effectively produce well-defined difference images where the boundary between foreground and background areas is clear. Furthermore, these methods exhibit remarkable superiority in their quantitative assessments. The NLMR gains the lowest FN (511) and competitive OA (0.9904), and $F1$ (0.8392) and κ (0.8342). The M2HG constructs a wide receptive field, thereby producing the lowest FP at 414. Moreover, compared with NLMR, its indicators of OA, $F1$, and κ surpass by 0.18%, 2.66%, and 2.76%, respectively.

It is noteworthy that the equivalent numbers of looks (ENLs) of the bitemporal SAR images in the Yellow River dataset are different, as shown in Table I. Specifically, the SAR image acquired in 2009 possesses an ENL of 1, inherently leading to a higher degree of speckle noise compared with the SAR image captured in 2008. This specific dataset offers an intricate noise environment, serving as an effective platform to assess the ability of various change detection methods to cope with noise

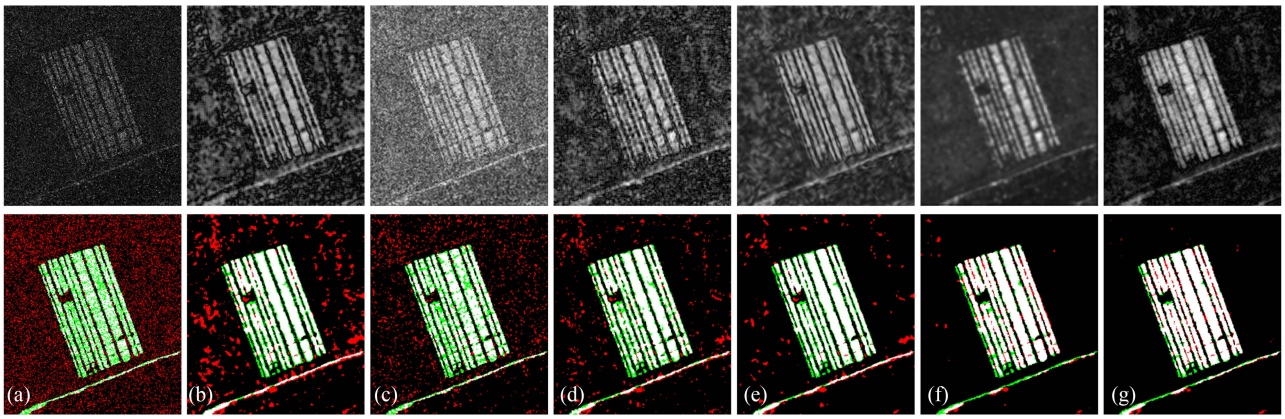

Fig. 10. Difference images (first row) and change maps (second row) of seven experimental methods on the Yellow River dataset. (a) LR. (b) MR. (c) NR. (d) DWT. (e) NLMR. (f) INLPG. (g) M2HG. In the change maps, White: TP; Black: TN; Green: FN; and Red: FP.

TABLE V
AVERAGE OF EVALUATION INDICATORS FOR CHANGE MEASURE METHODS

Method	OA	F1	κ	Time (s)
LR	0.9174	0.6632	0.6150	**1.11**
MR	0.9586	0.7979	0.7735	1.28
NR	0.9621	0.8176	0.7952	7.82
DWT	0.9676	0.8326	0.8136	9.29
NLMR	0.9754	0.8679	0.8535	3.02
INLPG	0.9778	0.8507	0.8380	37.88
M2HG	**0.9841**	**0.9013**	**0.8919**	449.02

interference. Therefore, the patch size of 7×7 is applied to all comparison methods. The qualitative results of seven change measure methods are shown in Fig. 10. In the change maps of LR, MR, NR, and DWT methods, a prevalence of red (FP) and green (FN) points is observed, indicating a substantial presence of misclassifications in their results. Although the NLMR method generally exhibits good noise resilience across other datasets, its performance on the Yellow River dataset yields less satisfactory results in terms of smoothness. The INLPG method produces a visually flat difference image, but it encounters limitations in identifying linear changed areas, which leads to a relatively high miss-detection rate. The proposed M2HG method generates a difference image with good separability, and the resulting change map accurately reflects real changes. Table IV provides the results of the quantitative analysis. The M2HG method achieves significant advantages on all indicators. The lowest FN and FP are obtained simultaneously. Compared with the second-best method, M2HG outperforms in terms of OA, κ, and $F1$ criteria by 1.24%, 3.76%, and 4.51%, respectively.

The statistical average of evaluation indicators for six datasets is presented in Table V. The LR method achieves the poorest performance, with an average κ value of merely 0.6150. The MR, NR, and DWT methods yield intermediate results, with $F1$ scores and κ coefficients oscillating around 0.8. The indicator averages of NLMR and INLPG are decent, with their average $F1$ exceeding 0.85. These results indicate that experimental methods employing nonlocal neighborhoods outperform those relying on local neighborhoods. Overall, both types of neighborhood-based experimental methods demonstrate superior performance compared with traditional pixel-based ones. The proposed M2HG method integrates multilevel neighborhood information, achieving an optimal average of all indicators. Compared with the suboptimal method, this method outperforms by 0.87%, 3.34%, and 3.84% for the OA, κ, and $F1$ indicators, respectively. Notably, the integrated application of multilevel neighborhood does introduce a higher time complexity, rendering M2HG the most time-consuming among the assessed methods.

In order to fully assess the difference image of M2HG, we plot the receiver operating characteristic (ROC) curve using the false alarm rate and good detection rate as horizontal and vertical axes [40]. ROC curves can evaluate the quality of a difference image regardless of the threshold. The larger the area between the curve and the horizontal axis, the better the quality of the generated difference image. ROC curves of the seven methods on the six datasets are plotted in Fig. 11. The blue curves, which represent the LR method, are consistently lower than the other curves due to their susceptibility to speckle noise. Beyond the red curves representing the M2HG method, an intertwining of differently colored curves suggests similarity in their respective performances. The red curves consistently position themselves closest to the top-left corner of the charts, suggesting the superiority of M2HG in change measure tasks. Based on the experimental analysis above, the proposed M2HG effectively aggregates the attributes of neighboring vertices along the multiorder and multilevel connections, and thus has good performance in terms of suppressing the speckle noise and retaining the edges of the changed area.

D. Parameters Analysis

In the aforementioned experiments on six datasets, the proposed M2HG method employs only two sets of parameters, with the same set of parameters consistently effective for five out of

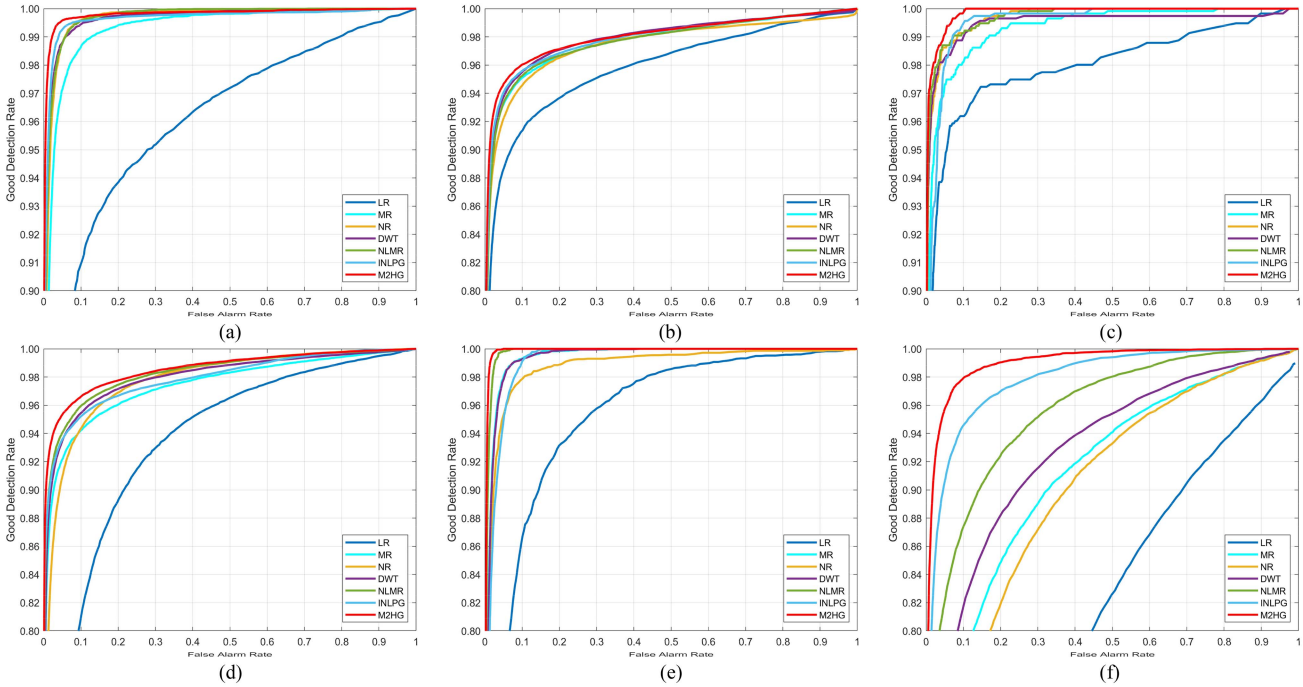

Fig. 11. ROC curves of the seven change measure methods. (a) Ottawa dataset. (b) Huai River dataset. (c) Bern dataset. (d) Lu'an dataset. (e) Vancouver dataset. (f) Yellow River dataset.

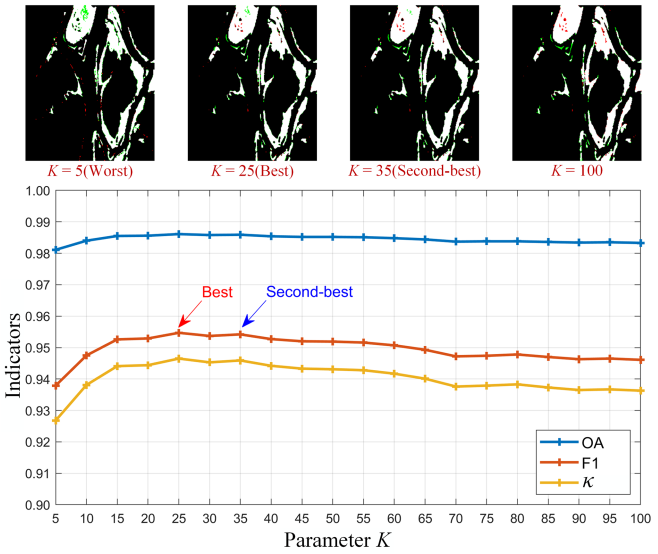

Fig. 12. Indicator curves of the proposed M2HG with different K on the Ottawa dataset.

these six datasets. This demonstrates the parameter insensitivity characteristic of the M2HG method. To further investigate the relationship between M2HG and its parameter setting, we systematically select K values at intervals of 5 within a range spanning from 5 to 100 and conduct parameter assessment experiments on the Ottawa dataset. The results of these experiments are presented in Fig. 12. The curves exhibit a relatively steady trend, providing empirical evidence for the robustness and stability of the proposed M2HG method. Overall, the curves are characterized by an initial increase and subsequent decrease with the increment of parameter K. The lowest performance indicators (OA $= 0.9811$; $F1 = 0.9379$; and $\kappa = 0.9268$) are observed at the initial point with $K = 5$.

The corresponding change map reveals a considerable amount of errors, as evidenced by the widespread distribution of red and green markers across both unchanged and changed areas. The indicators of the final point ($\kappa = 100$) are also unsatisfactory, as the oversmoothing effect leads to the erosion of small changed areas within the change map. The optimal performance (OA $=$ 0.9861; $F1 = 0.9547$; and $\kappa = 0.9465$) is achieved when $K =$ 25, and the indicator values of its adjacent points also present decent results. For example, the second-best indicators (OA $=$ 0.9859; $F1 = 0.9542$; and $\kappa = 0.9459$) occur at $K = 35$. From the experiments, it is evident that K values within the range of 15–60 are advantageous for the proposed M2HG method when applied to change detection tasks on the Ottawa dataset. Importantly, this range aligns well with the recommended parameter setting interval.

E. Analysis of Change Detection Results

In the second experiment, comparative assessments are conducted among several competing methods, namely GC, PCA-K, MRFFCM, PCANet, and CWNN, along with hybrid methods M2HG-GC and M2HG-CWNN. The final change maps for six SAR datasets are shown in Fig. 13. Quantitative evaluations are exhibited in Table VI. The change maps produced by MRFFCM often display chaotic patterns, characterized by a mass of incorrect detections appeared in the unchanged areas. This issue is particularly apparent in the Ottawa, Bern, Huai

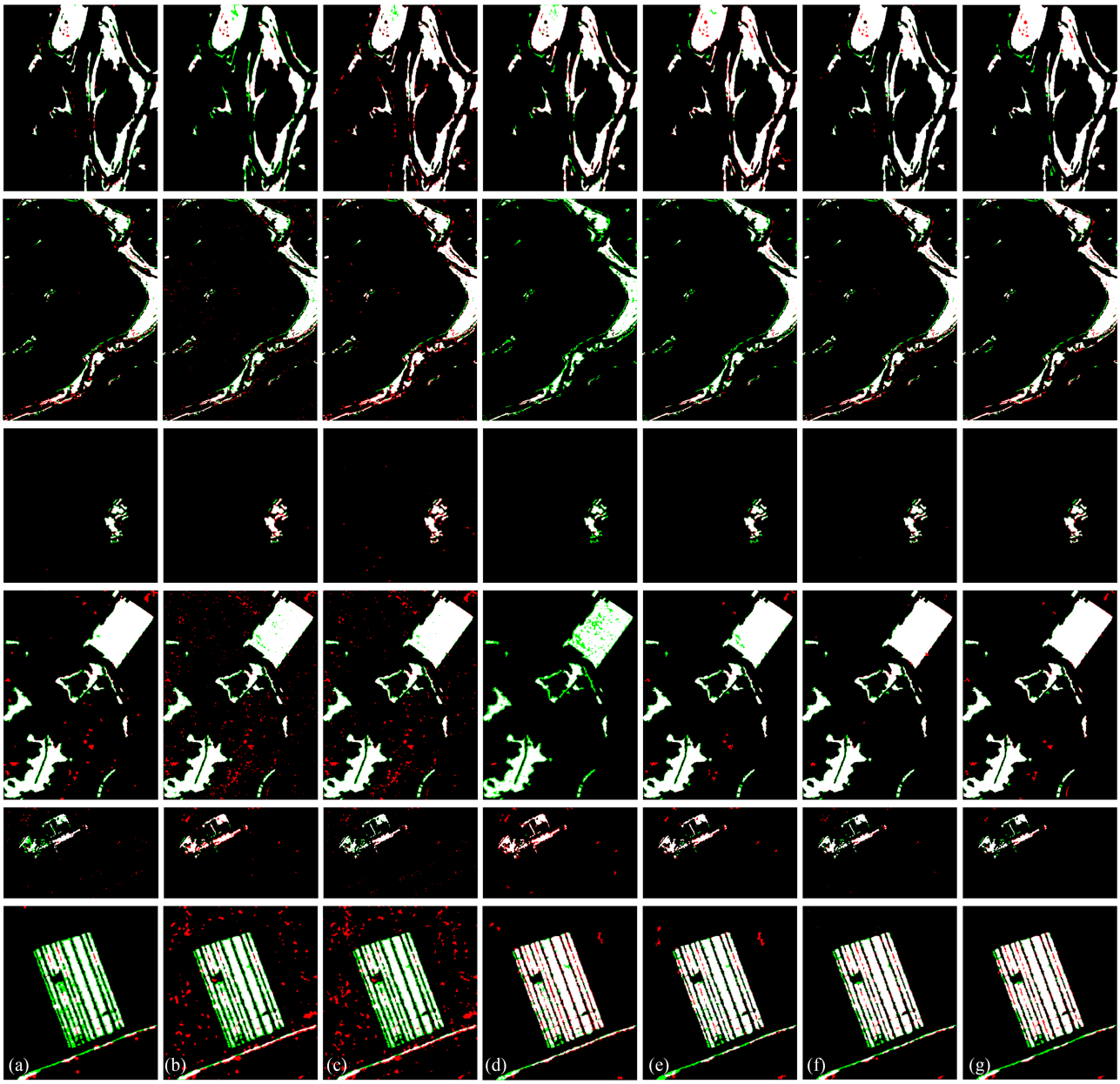

Fig. 13. Results of seven change detection methods on the Ottawa dataset (first row), Huai river dataset (second row), Bern dataset (third row), Lu'an dataset (fourth row), Vancouver dataset (fifth row), and Yellow river dataset (last row). (a) GC. (b) PCA-K. (c) MRFFCM. (d) PCANet. (e) CWNN. (f) M2HG-GC. (g) M2HG-CWNN. In the change maps, White: TP; Black: TN; Green: FN; and Red: FP.

River, and Yellow River datasets, resulting in the MRFFCM achieving the highest FP among the evaluated methods. The PCA-K method produces decent change detection results on the Ottawa and Bern datasets, which is attributed to the high ENL in the SAR images. However, when dealing with datasets featuring lower ENL, the change maps generated by PCA-K display numerous red spots in the unchanged areas, concurrent with declines in performance indicators. This indicates a limited capacity for noise suppression. The GC method is effective in noise suppression due to its efficient use of spatial information. The corresponding change maps are typically flat, with some red blocks appearing only in the Lu'an dataset. The PCANet outcomes exhibit marked instability across different datasets. Specifically, it struggles with significant miss detections in the Lu'an and Huai River datasets, leading to the highest FN. Conversely, in the Vancouver dataset, PCANet records the highest FP. This polarized performance could potentially stem from the inaccuracy of preceding clustering and the instability of pseudolabel training. The CWNN method yields good results, but the descriptions of changed areas are not precise enough. The hybrid M2HG-GC and M2HG-CWNN methods produce satisfactory change maps, with only a few red points appearing in the unchanged areas. They achieve the highest OA, κ, and $F1$, demonstrating their superiority in describing changes. Compared with the GC method, the M2HG-GC achieves an average improvement of 5.93% and 6.57% in $F1$ and κ metrics,

TABLE VI
RESULTS OF SEVEN CHANGE DETECTION METHODS

Dataset	Method	FN	FP	OA	F1	κ
Ottawa	GC	1129	501	0.9839	0.9482	0.9387
	PCA-K	2103	**462**	0.9747	0.9158	0.9010
	MRFFCM	**388**	1600	0.9804	0.9403	0.9286
	PCANet	987	1056	0.9799	0.9365	0.9245
	CWNN	462	1489	0.9808	0.9411	0.9296
	M2HG-GC	551	596	**0.9887**	**0.9643**	**0.9576**
	M2HG-CWNN	696	575	0.9875	0.9603	0.9528
Huai river	GC	4897	4006	0.9790	0.8640	0.8527
	PCA-K	5190	3768	0.9789	0.8621	0.8506
	MRFFCM	**3301**	6788	0.9762	0.8556	0.8426
	PCANet	10760	**448**	0.9736	0.8000	0.7864
	CWNN	6546	1575	0.9809	0.8677	0.8575
	M2HG-GC	4036	3395	0.9825	0.8869	0.8774
	M2HG-CWNN	3671	3677	**0.9827**	**0.8893**	**0.8799**
Bern	GC	255	74	0.9964	0.8455	0.8436
	PCA-K	123	247	0.9959	0.8480	0.8459
	MRFFCM	**55**	407	0.9949	0.8264	0.8239
	PCANet	383	**39**	0.9953	0.7854	0.7831
	CWNN	224	86	0.9966	0.8573	0.8555
	M2HG-GC	153	120	**0.9970**	**0.8801**	**0.8786**
	M2HG-CWNN	134	145	0.9969	0.8798	0.8782
Lu'an	GC	3699	2416	0.9754	0.9177	0.9032
	PCA-K	3650	4537	0.9671	0.8929	0.8735
	MRFFCM	3715	4466	0.9671	0.8928	0.8734
	PCANet	9665	**90**	0.9608	0.8521	0.8301
	CWNN	3559	1094	0.9813	0.9363	0.9254
	M2HG-GC	2665	708	**0.9864**	**0.9542**	**0.9462**
	M2HG-CWNN	**2228**	1529	0.9849	0.9498	0.9409
Vancouver	GC	998	495	0.9876	0.7733	0.7670
	PCA-K	337	1514	0.9847	0.7761	0.7683
	MRFFCM	517	760	0.9894	0.8259	0.8204
	PCANet	**67**	1987	0.9830	0.7720	0.7636
	CWNN	224	928	0.9905	0.8522	0.8473
	M2HG-GC	344	534	0.9927	**0.8794**	**0.8757**
	M2HG-CWNN	500	**361**	**0.9929**	0.8761	0.8725
Yellow river	GC	4179	1358	0.9255	0.7697	0.7260
	PCA-K	3636	2373	0.9191	0.7653	0.7166
	MRFFCM	3850	3192	0.9052	0.7313	0.6738
	PCANet	1214	1970	0.9571	0.8847	0.8584
	CWNN	1592	**902**	0.9664	0.9047	0.8844
	M2HG-GC	1449	943	**0.9678**	**0.9092**	**0.8897**
	M2HG-CWNN	**1213**	1241	0.9670	0.9087	0.8886

respectively. Similarly, compared with the CWNN method, the M2HG-CWNN shows an average enhancement of 1.75% and 1.89% on the $F1$ and κ criteria, respectively. The results of these combined methods illustrate the effectiveness of the difference images obtained by the proposed M2HG. Meanwhile, these results also imply that, for boosting the accuracy of change detection, a method capable of generating difference images with good separability is equally important as any promising change analysis method.

IV. CONCLUSION

This study proposes an M2HG method for change detection between bitemporal SAR images. This method highlights the use of multiorder and multilevel neighborhood information to guide change measure. In detail, we establish the local, nonlocal, and global connections according to three adjacency rules. Then, a novel heterogeneous graph is constructed by assigning different weights to these multilevel connections. With the support of heterogeneous graph, the CRWM is presented to quantify these multilevel connections. Thereafter, the heterogeneous graph shift system, which consists of the multiorder CRWM, is designed to aggregate the attributes of neighboring vertices along the multiorder and multilevel connections. The change measure can be implemented by comparing the output signals through the heterogeneous graph shift systems, and thus generating the difference image with good separability. Compared with other neighborhood-based change measure methods, the M2HG provides a wider and deeper receptive field through multiorder and multilevel connections. The local and nonlocal connections are designed for speckle suppression and the global connection is constructed for changes amplification. Therefore, the proposed M2HG performs well in both speckle noise suppression and change detail preservation. Experiments conducted on six real SAR datasets present that the proposed M2HG outperforms other optimal change measure methods in terms of OA, κ, and $F1$ criteria by 0.87%, 3.34%, and 3.84%, respectively. In addition, the combination of M2HG with a superior classifier has been evidenced to elevate the change detection accuracy. This emphasizes the pivotal role played by difference images with good separability in achieving superior change detection outcomes.

Future work may develop the graph structure of M2HG to GCs or graph neural network for image classification and change analysis. The combination of imaging invariant feature with M2HG can also be investigated to perform multimodal change detection tasks. In addition, due to the complicated structure of heterogeneous graph and shift system, the time complexity for M2HG to compute the $H(\mathbf{P}_{\mathrm{HG}})\mathbf{f}$ is $O(N^4)$. Therefore, another perspective for future work involves applying nonoverlapping patches or superpixels to heterogeneous graphs. This would effectively reduce the number of vertices and alleviate the computational complexity at the same time.

REFERENCES

[1] W. Shi, M. Zhang, R. Zhang, S. Chen, and Z. Zhan, "Change detection based on artificial intelligence: State-of-the-art and challenges," *Remote Sens.*, vol. 12, no. 10, May 2020, Art. no. 1688.
[2] K. Wessels et al., "Quantifying the sensitivity of L-band SAR to a decade of vegetation structure changes in savannas," *Remote Sens. Environ.*, vol. 284, Jan. 2023, Art. no. 113369.
[3] H. Wang, X. Lv, and S. Li, "A new building change detection method based on cross-temporal stereo matching using satellite stereo imagery," *IEEE Geosci. Remote Sens. Lett.*, vol. 20, Sep. 2023, Art. no. 6011305.

[4] J. Li, Z. Li, H. Wu, and N. You, "Trend, seasonality, and abrupt change detection method for land surface temperature time-series analysis: Evaluation and improvement," *Remote Sens. Environ.*, vol. 280, Oct. 2022, Art. no. 113222.
[5] Z. Li, W. Shi, S. W. Myint, P. Lu, and Q. Wang, "Semi-automated landslide inventory mapping from bitemporal aerial photographs using change detection and level set method," *Remote Sens. Environ.*, vol. 175, pp. 215–230, Mar. 2016.
[6] X. Li et al., "Spatial-temporal super-resolution land cover mapping with a local spatial-temporal dependence model," *IEEE Trans. Geosci. Remote Sens.*, vol. 57, no. 7, pp. 4951–4966, Jul. 2019.
[7] H. Fang, S. Guo, X. Wang, S. Liu, C. Lin, and P. Du, "Automatic urban scene-level binary change detection based on a novel sample selection approach and advanced triplet neural network," *IEEE Trans. Geosci. Remote Sens.*, vol. 61, Jan. 2023, Art. no. 5601518.
[8] J. Lu, J. Li, G. Chen, L. Zhao, B. Xiong, and G. Kuang, "Improving pixel-based change detection accuracy using an object-based approach in multitemporal SAR flood images," *IEEE J. Sel. Topics Appl. Earth Observ. Remote Sens.*, vol. 8, no. 7, pp. 3486–3496, Jul. 2015.
[9] J. Alatalo, T. Sipola, and M. Rantonen, "Improved difference images for change detection classifiers in SAR imagery using deep learning," *IEEE Trans. Geosci. Remote Sens.*, vol. 61, Oct. 2023, Art. no. 5218714.
[10] M. Gong, Y. Li, L. Jiao, M. Jia, and L. Su, "SAR change detection based on intensity and texture changes," *ISPRS J. Photogramm. Remote Sens.*, vol. 93, pp. 123–135, Jul. 2014.
[11] Y. Bazi, L. Bruzzone, and F. Melgani, "An unsupervised approach based on the generalized Gaussian model to automatic change detection in multitemporal SAR images," *IEEE Trans. Geosci. Remote Sens.*, vol. 43, no. 4, pp. 874–887, Apr. 2005.
[12] E. J. M. Rignot and J. J. van Zyl, "Change detection techniques for ERS-1 SAR data," *IEEE Trans. Geosci. Remote Sens.*, vol. 31, no. 4, pp. 896–906, Jul. 1993.
[13] M. Gong, Y. Cao, and Q. Wu, "A neighborhood-based ratio approach for change detection in SAR images," *IEEE Geosci. Remote Sens. Lett.*, vol. 9, no. 2, pp. 307–311, Mar. 2012.
[14] J. Ma, M. Gong, and Z. Zhou, "Wavelet fusion on ratio images for change detection in SAR images," *IEEE Geosci. Remote Sens. Lett.*, vol. 9, no. 6, pp. 1122–1126, Nov. 2012.
[15] M. Gong, Z. Zhou, and J. Ma, "Change detection in synthetic aperture radar images based on image fusion and fuzzy clustering," *IEEE Trans. Image Process.*, vol. 21, no. 4, pp. 2141–2151, Apr. 2012.
[16] J. Inglada, "Change detection on SAR images by using a parametric estimation of the Kullback-Leibler divergence," in *Proc. IEEE Int. Geosci. Remote Sens. Symp.*, 2003, vol. 6, pp. 4104–4106.
[17] J. Inglada and G. Mercier, "A new statistical similarity measure for change detection in multitemporal SAR images and its extension to multiscale change analysis," *IEEE Trans. Geosci. Remote Sens.*, vol. 45, no. 5, pp. 1432–1445, May 2007.
[18] T. Tasdizen, "Principal neighborhood dictionaries for nonlocal means image denoising," *IEEE Trans. Image Process.*, vol. 18, no. 12, pp. 2649–2660, Dec. 2009.
[19] L. Su, M. Gong, and B. Sun, "Change detection in synthetic aperture radar images based on non-local means with ratio similarity measurement," *Int. J. Remote Sens.*, vol. 35, no. 22, pp. 7673–7690, Nov. 2014.
[20] H. Zhuang, M. Hao, K. Deng, K. Zhang, X. Wang, and G. Yao, "Change detection in SAR images via ratio-based Gaussian kernel and nonlocal theory," *IEEE Trans. Geosci. Remote Sens.*, vol. 60, Jan. 2022, Art. no. 5210215.
[21] J. Wang, X. Yang, X. Yang, L. Jia, and S. Fang, "Unsupervised change detection between SAR images based on hypergraphs," *ISPRS J. Photogramm. Remote Sens.*, vol. 164, pp. 61–72, Jun. 2020.
[22] J. Wang, X. Yang, L. Jia, X. Yang, and Z. Zhang, "Pointwise SAR image change detection using stereo-graph cuts with spatio-temporal information," *Remote Sens. Lett.*, vol. 10, no. 5, pp. 421–429, Jan. 2019.
[23] Y. Sun, L. Lei, X. Li, X. Tan, and G. Kuang, "Patch similarity graph matrix-based unsupervised remote sensing change detection with homogeneous and heterogeneous sensors," *IEEE Trans. Geosci. Remote Sens.*, vol. 59, no. 6, pp. 4841–4861, Jun. 2021.
[24] R. Wang, L. Wang, X. Wei, J.-W. Chen, and L. Jiao, "Dynamic graph-level neural network for SAR image change detection," *IEEE Geosci. Remote Sens. Lett.*, vol. 19, Jan. 2022, Art. no. 4501005.
[25] M.-T. Pham, G. Mercier, and J. Michel, "Change detection between SAR images using a pointwise approach and graph theory," *IEEE Trans. Geosci. Remote Sens.*, vol. 54, no. 4, pp. 2020–2032, Apr. 2016.
[26] J. Wang, X. Yang, and L. Jia, "Pointwise SAR image change detection based on stereograph model with multiple-span neighbourhood information," *Int. J. Remote Sens.*, vol. 40, no. 1, pp. 31–50, Jan. 2019.
[27] J. Wang, T. Zhao, and X. Jiang, "Unsupervised multi-look SAR image change detection driven by dual-layer graph with intensity and texture attributes," *IEEE Geosci. Remote Sens. Lett.*, vol. 19, Jan. 2022, Art. no. 4502705.
[28] Y. Sun, L. Lei, X. Li, X. Tan, and G. Kuang, "Structure consistency-based graph for unsupervised change detection with homogeneous and heterogeneous remote sensing images," *IEEE Trans. Geosci. Remote Sens.*, vol. 60, Dec. 2021, Art. no. 4700221.
[29] A. Salim, S. S. Shiju, and S. Sumitra, "Neighborhood preserving kernels for attributed graphs," *IEEE Trans. Pattern Anal. Mach. Intell.*, vol. 45, no. 1, pp. 828–840, Jan. 2023.
[30] Q. Wang, Y. Miao, M. Chen, and Y. Yuan, "Spatial-spectral clustering with anchor graph for hyperspectral image," *IEEE Trans. Geosci. Remote Sens.*, vol. 60, Oct. 2022, Art. no. 5542413.
[31] S. Liu, L. Duan, Z. Zhang, X. Cao, and T. S. Durrani, "Ground-based remote sensing cloud classification via context graph attention network," *IEEE Trans. Geosci. Remote Sens.*, vol. 60, Dec. 2022, Art. no. 5602711.
[32] Q. Liu, L. Xiao, J. Yang, and Z. Wei, "Multilevel superpixel structured graph U-nets for hyperspectral image classification," *IEEE Trans. Geosci. Remote Sens.*, vol. 60, Jan. 2022, Art. no. 5516115.
[33] Z. Song, X. Yang, Z. Xu, and I. King, "Graph-based semi-supervised learning: A comprehensive review," *IEEE Trans. Neural Netw. Learn. Syst.*, vol. 34, no. 11, pp. 8174–8194, Nov. 2023.
[34] J. Wang and A. Zhang, "SAR image change detection based on heterogeneous graph with multiattributes and multirelationships," *IEEE Access*, vol. 10, pp. 44347–44361, 2022.
[35] J. Wang, T. Zhao, X. Jiang, and K. Lan, "A hierarchical heterogeneous graph for unsupervised SAR image change detection," *IEEE Geosci. Remote Sens. Lett.*, vol. 19, Nov. 2022, Art. no. 4516605.
[36] Y. Sun, D. Zhu, H. Du, and Z. Tian, "MHNF: Multi-hop heterogeneous neighborhood information fusion graph representation learning," *IEEE Trans. Knowl. Data Eng.*, vol. 35, no. 7, pp. 7192–7205, Jul. 2023.
[37] E. Elhamifar and R. Vidal, "Sparse subspace clustering: Algorithm, theory, and applications," *IEEE Trans. Pattern Anal. Mach. Intell.*, vol. 35, no. 11, pp. 2765–2781, Nov. 2013.
[38] C. Deledalle, L. Denis, and F. Tupin, "Iterative weighted maximum likelihood denoising with probabilistic patch-based weights," *IEEE Trans. Image Process.*, vol. 18, no. 12, pp. 2661–2672, Dec. 2009.
[39] N. Otsu, "A threshold selection method from gray-level histograms," *IEEE Trans. Syst., Man, Cybern.*, vol. 9, no. 1, pp. 62–66, Jan. 1979.
[40] J. Kerekes, "Receiver operating characteristic curve confidence intervals and regions," *IEEE Geosci. Remote Sens. Lett.*, vol. 5, no. 2, pp. 251–255, Apr. 2008.
[41] Y. Boykov and V. Kolmogorov, "An experimental comparison of mincut/max-flow algorithms for energy minimization in vision," *IEEE Trans. Pattern Anal. Mach. Intell.*, vol. 26, no. 9, pp. 1124–1137, Sep. 2004.
[42] T. Celik, "Unsupervised change detection in satellite images using principal component analysis and K-means clustering," *IEEE Geosci. Remote Sens. Lett.*, vol. 6, no. 4, pp. 772–776, Oct. 2009.
[43] M. Gong, L. Su, M. Jia, and W. Chen, "Fuzzy clustering with a modified MRF energy function for change detection in synthetic aperture radar images," *IEEE Trans. Fuzzy Syst.*, vol. 22, no. 1, pp. 98–109, Feb. 2014.
[44] J. Dong, B. Li, and Q. Xu, "Automatic change detection in synthetic aperture radar images based on PCANet," *IEEE Geosci. Remote Sens. Lett.*, vol. 13, no. 12, pp. 1792–1796, Dec. 2016.
[45] F. Gao, X. Wang, Y. Gao, J. Dong, and S. Wang, "Sea ice change detection in SAR images based on convolutional-wavelet neural networks," *IEEE Geosci. Remote Sens. Lett.*, vol. 16, no. 8, pp. 1240–1244, Aug. 2019.

Jun Wang (Member, IEEE) received the M.S. degree in computer technology from the Anhui University of Technology, Ma'anshan, China, in 2013, and the Ph.D. degree in signal and information processing from the Hefei University of Technology, Hefei, China, in 2020.

He is currently an Associate Professor with the School of Mechanical Engineering, Quzhou University, Quzhou, China. His current research interests include computer vision, machine learning, and change detection.

Fei Zeng received the B.S. degree in mechanical design, manufacturing, and automation from the Jiangxi University of Science and Technology, Ganzhou, China, in 2022. He is currently working toward the M.S. degree in mechanical engineering with the Zhejiang University of Technology, Hangzhou, China.

His current research interests include image processing and change detection.

Sanku Niu received the M.S. and Ph.D. degrees in armament science and technology from the Beijing Institute of Technology, Beijing, China, in 2011 and 2016, respectively.

He is currently a Senior Engineer with the School of Mechanical Engineering, Quzhou University, Quzhou, China. His current research interests include computer vision and agricultural robot.

Jun Zheng received the M.S. degree in information and communication engineering from Chang'an University, Xi'an, China, in 2019.

He is currently a Teaching Assistant with the School of Information Engineering, Huangshan University, Huangshan City, China. His current research interests include radar signal processing and image processing.

Xiaoliang Jiang received the M.S. and Ph.D. degrees in mechanical design from Southwest Jiaotong University, Chengdu, China, in 2013 and 2016, respectively.

He is currently a Professor with the School of Mechanical Engineering, Quzhou University, Quzhou, China. His research interests include machine vision and image recognition.